

# Photoacoustic microscopy *in vivo* using synthetic-aperture focusing technique combined with three-dimensional deconvolution

DE CAI,<sup>1</sup> ZHONGFEI LI,<sup>1</sup> YAO LI,<sup>1</sup> ZHENDONG GUO,<sup>1</sup> AND SUNG-LIANG CHEN<sup>1,2,\*</sup>

<sup>1</sup>University of Michigan-Shanghai Jiao Tong University Joint Institute, Shanghai Jiao Tong University, Shanghai 200240, China

<sup>2</sup>State Key Laboratory of Advanced Optical Communication Systems and Networks, Shanghai Jiao Tong University, Shanghai 200240, China

\*[sungliang.chen@sjtu.edu.cn](mailto:sungliang.chen@sjtu.edu.cn)

**Abstract:** Acoustic-resolution photoacoustic microscopy (ARPAM) plays an important role in studying the microcirculation system of biological tissues with deep penetration. High lateral resolution of ARPAM is achieved by using a high numerical aperture acoustic transducer. The deteriorated lateral resolution in the out-of-focus region can be alleviated by synthetic aperture focusing technique (SAFT). Previously, we reported a three-dimensional (3D) deconvolution ARPAM to improve both lateral and axial resolutions in the focus region. In this study, we present our extension of resolution enhancement to the out-of-focus region based on two-dimensional SAFT combined with the 3D deconvolution (SAFT+Deconv). In both the focus and out-of-focus regions, depth-independent lateral resolution provided by SAFT, together with inherently depth-independent axial resolution, ensures a depth-independent point spread function for 3D deconvolution algorithm. Imaging of 10  $\mu\text{m}$  polymer beads shows that SAFT+Deconv ARPAM improves the  $-6$  dB lateral resolutions from 65–700  $\mu\text{m}$  to 20–29  $\mu\text{m}$ , and the  $-6$  dB axial resolutions from 35–42  $\mu\text{m}$  to 12–19  $\mu\text{m}$  in an extended depth of focus (DOF) of  $\sim 2$  mm. The signal-to-noise ratio is also increased by 6–30 dB. The resolution enhancement in three dimensions is validated by *in vivo* imaging of a mouse's dorsal subcutaneous microvasculature. Our results suggest that SAFT+Deconv ARPAM may allow fine spatial resolution with deep penetration and extended DOF for biomedical photoacoustic applications.

© 2017 Optical Society of America

**OCIS codes:** (170.3880) Medical and biological imaging; (170.5120) Photoacoustic imaging; (170.6900) Three-dimensional microscopy; (100.1830) Deconvolution.

## References and links

1. L. V. Wang, "Multiscale photoacoustic microscopy and computed tomography," *Nat. Photonics* **3**(9), 503–509 (2009).
2. L. V. Wang and S. Hu, "Photoacoustic tomography: in vivo imaging from organelles to organs," *Science* **335**(6075), 1458–1462 (2012).
3. K. Maslov, H. F. Zhang, S. Hu, and L. V. Wang, "Optical-resolution photoacoustic microscopy for in vivo imaging of single capillaries," *Opt. Lett.* **33**(9), 929–931 (2008).
4. V. Ntziachristos, "Going deeper than microscopy: the optical imaging frontier in biology," *Nat. Methods* **7**(8), 603–614 (2010).
5. S.-L. Chen, Z. Xie, P. L. Carson, X. Wang, and L. J. Guo, "In vivo flow speed measurement of capillaries by photoacoustic correlation spectroscopy," *Opt. Lett.* **36**(20), 4017–4019 (2011).
6. T. J. Allen, A. Hall, A. P. Dhillon, J. S. Owen, and P. C. Beard, "Spectroscopic photoacoustic imaging of lipid-rich plaques in the human aorta in the 740 to 1400 nm wavelength range," *J. Biomed. Opt.* **17**(6), 0612091 (2012).
7. K. Jansen, A. F. Van Der Steen, H. M. van Beusekom, J.W. Oosterhuis, and G. van Soest, "Intravascular photoacoustic imaging of human coronary atherosclerosis," *Opt. Lett.* **36**(5), 597–599 (2011).
8. S. Sethuraman, J. H. Amirian, S. H. Litovsky, R. W. Smalling, and S. Y. Emelianov, "Spectroscopic intravascular photoacoustic imaging to differentiate atherosclerotic plaques," *Opt. Express* **16**(5), 3362–3367 (2008).
9. J.-M. Yang, C. Favazza, R. Chen, J. Yao, X. Cai, K. Maslov, Q. Zhou, K. K. Shung, and L. V. Wang, "Simultaneous functional photoacoustic and ultrasonic endoscopy of internal organs in vivo," *Nat. Med.* **18**(8), 1297–1302 (2012).
10. P. Wang, T. Ma, M. N. Slipchenko, S. Liang, J. Hui, K. K. Shung, S. Roy, M. Sturek, Q. Zhou, Z. Chen and J.-X. Cheng, "High-speed intravascular photoacoustic imaging of lipid-laden atherosclerotic plaque enabled by a 2-kHz barium nitrate raman laser," *Sci. Rep.* **4**, 6889 (2014).

11. W. Song, W. Zheng, R. Liu, R. Lin, H. Huang, X. Gong, S. Yang, R. Zhang, and L. Song, "Reflection-mode in vivo photoacoustic microscopy with subwavelength lateral resolution," *Biomed. Opt. Express* **5**(12), 4235–4241 (2014).
12. K. Maslov, G. Stoica, and L. V. Wang, "In vivo dark-field reflection-mode photoacoustic microscopy," *Opt. Lett.* **30**(6), 625–627 (2005).
13. H. F. Zhang, K. Maslov, G. Stoica, and L. V. Wang, "Functional photoacoustic microscopy for high-resolution and noninvasive in vivo imaging," *Nat. Biotechnol.* **24**(7), 848–851 (2006).
14. K. H. Song, E. W. Stein, J. A. Margenthaler, and L. V. Wang, "Noninvasive photoacoustic identification of sentinel lymph nodes containing methylene blue in vivo in a rat model," *J. Biomed. Opt.* **13**(5), 054033 (2008).
15. R. Ma, S. Söntges, S. Shoham, V. Ntziachristos, and D. Razansky, "Fast scanning coaxial optoacoustic microscopy," *Biomed. Opt. Express* **3**(7), 1724–1731 (2012).
16. C.-K. Liao, M.-L. Li, and P.-C. Li, "Optoacoustic imaging with synthetic aperture focusing and coherence weighting," *Opt. Lett.* **29**(21), 2506–2508 (2004).
17. M.-L. Li, H. F. Zhang, K. Maslov, G. Stoica, and L. V. Wang, "Improved in vivo photoacoustic microscopy based on a virtual-detector concept," *Opt. Lett.* **31**(4), 474–476 (2006).
18. Z. Deng, X. Yang, H. Gong, and Q. Luo, "Two-dimensional synthetic-aperture focusing technique in photoacoustic microscopy," *J. Appl. Phys.* **109**(10), 104701 (2011).
19. Z. Deng, X. Yang, H. Gong, and Q. Luo, "Adaptive synthetic-aperture focusing technique for microvasculature imaging using photoacoustic microscopy," *Opt. Express* **20**(7), 7555–7563 (2012).
20. J. Turner, H. Estrada, M. Kneipp, and D. Razansky, "Improved optoacoustic microscopy through three-dimensional spatial impulse response synthetic aperture focusing technique," *Opt. Lett.* **39**(12), 3390–3393 (2014).
21. K. H. Song, E. W. Stein, J. A. Margenthaler, and L. V. Wang, "Delay-multiply-and-sum-based synthetic aperture focusing in photoacoustic microscopy," *J. Biomed. Opt.* **21**(3), 036010 (2016).
22. S. I. Nikolov and J. A. Jensen, "3D synthetic aperture imaging using a virtual source element in the elevation plane," in *Proceedings of IEEE Conference on Ultrasonics* (Institute of Electrical and Electronics Engineers, 2000), pp. 1743–1747.
23. H. F. Zhang, K. Maslov, M.-L. Li, G. Stoica, and L. V. Wang, "In vivo volumetric imaging of subcutaneous microvasculature by photoacoustic microscopy," *Opt. Express* **14**(20), 9317–9323 (2006).
24. C. Yu, C. Zhang, and L. Xie, "A blind deconvolution approach to ultrasound imaging," *IEEE Trans. Ultrason. Ferroelectr. Freq. Control* **59**(2), 271–280 (2012).
25. Y. Liu, Y. Liang, G. Mu, and X. Zhu, "Deconvolution methods for image deblurring in optical coherence tomography," *J. Opt. Soc. Am. A* **26**(1), 72–77 (2009).
26. J. Chen, R. Lin, H. Wang, J. Meng, H. Zheng, and L. Song, "Blind-deconvolution optical-resolution photoacoustic microscopy in vivo," *Opt. Express* **59**(2), 7316–7327 (2013).
27. D. Cai, Z. Li, and S.-L. Chen, "In vivo deconvolution acoustic-resolution photoacoustic microscopy in three dimensions," *Biomed. Opt. Express* **7**(2), 369–380 (2016).
28. C. Preza and J.-A. Conchello, "Depth-variant maximum-likelihood restoration for three-dimensional fluorescence microscopy," *J. Opt. Soc. Am. A* **21**(9), 1593–1601 (2004).
29. J. Kim, S. An, S. Ahn, and B. Kim, "Depth-variant deconvolution of 3D widefield fluorescence microscopy using the penalized maximum likelihood estimation method," *Opt. Express* **21**(23), 27668–27681 (2013).
30. B. Piwakowski and B. Delannoy, "Method for computing spatial pulse response: Time-domain approach," *J. Acoust. Soc. Am.* **86**(6), 2422–2432 (1989).
31. W. H. Richardson, "Bayesian-based iterative method of image restoration," *J. Opt. Soc. Am. A* **62**(1), 55–59 (1972).
32. L. B. Lucy, "An iterative technique for the rectification of observed distributions," *Astronomical J.* **79**, 745 (1974).
33. R. L. White, "Image restoration using the damped richardson-lucy method," *Proc. SPIE* **2198**, 1342–1348 (1994).
34. M., Laasmaa, M., Vendelin, and P., Peterson, "Application of regularized Richardson Lucy algorithm for deconvolution of confocal microscopy images," *J. Microsc.* **243**(2), 124–140 (2011).

## 1. Introduction

The past decade has seen tremendous progress in photoacoustic (PA) imaging [1, 2]. In PA imaging, a short laser pulse is used to irradiate biological tissue. Then, a small temperature rise induced by the absorption of laser pulse gives rise to transient thermoelastic expansion and the emission of ultrasonic waves, also called PA waves. The detected PA signals are used to map optical absorption distribution within the biological tissue. PA imaging uniquely combines high optical contrast and low acoustic scattering. As an emerging hybrid imaging modality, it has found wide biomedical applications, including imaging of microcirculation [3–5], atherosclerotic vulnerable plaque identification [6–8], and endoscopic imaging [9, 10].

Two types of PA microscopy (PAM) can be implemented to achieve high-resolution either by optical focusing [3, 11] or acoustic focusing [12–14], referred to as optical-resolution PAM (ORPAM) and acoustic-resolution PAM (ARPAM), respectively. ORPAM can achieve lateral

resolution in several micrometers or even sub-micrometer by employing tight optical focusing. However, optical focusing becomes ineffective beyond optical diffusion limit ( $\sim 1$  mm below human skin) [1]. High lateral resolution of ARPAM is achieved by utilizing ultrasonic transducers with high center frequency and high numerical aperture (NA). A penetration depth of 6 mm has been demonstrated as the scattering of ultrasound in tissues is 2–3 orders of magnitude weaker than that of light [15]. There are, however, challenges for high-resolution ARPAM: (i) Higher-frequency ultrasound waves attenuate sharply in biological tissue; (ii) Depth-of-focus (DOF) of a focused ultrasonic transducer shrinks quickly with increased acoustic NA. Therefore, high lateral resolution is guaranteed only in limited focus region. For example, a focused ultrasonic transducer with a center frequency of 50 MHz and an NA of 0.44 has a DOF about 300  $\mu\text{m}$ .

The degraded lateral resolution of ARPAM in the out-of-focus region can be improved by synthetic aperture focusing technique (SAFT). Liao *et al.* first proposed the idea of SAFT, using a needle hydrophone, to improve the resolution and the signal-to-noise ratio (SNR) in PA imaging [16]. Then Li *et al.* further developed virtual-point detector (VPD) SAFT where a high NA focused transducer can be applied [17]. Afterwards, SAFT was naturally extended to two dimensional (2D) implementation by Deng *et al.* to yield isotropic lateral resolution [18]. Adaptive SAFT was also implemented to get better imaging of out-of-focus vessels by combining 2D SAFT and 1D SAFT [19]. More recently spatial impulse response (SIR) of a transducer was introduced to weight the spatial contributions in SAFT algorithm so that SAFT can be applied to the focus region [20]. Delay-multiply-and-sum-based synthetic aperture focusing [21] was also reported by Park *et al.*. Depth-independent lateral resolution in SAFT images was demonstrated both in ultrasound imaging [22] and PA imaging [17, 23]. The axial resolution of ARPAM, determined by the bandwidth of an ultrasonic transducer, is inherently depth independent.

Deconvolution algorithm for resolution enhancement has been widely exploited in ultrasound imaging [24], optical coherence tomography [25], and PA imaging [26, 27]. Deconvolution algorithm using depth-dependent point spread functions (PSFs) is also exploited in fluorescence microscopy [28, 29], measuring so many PSFs in different layers, however, is still a challenging task. Previously we developed three-dimensional (3D) deconvolution ARPAM to enhance lateral and axial resolution [27], yet the resolution enhancement is performed only in the focus region because the measured PSF for deconvolution in the focus region is different from that in the out-of-focus region.

In this work, we combine 2D SAFT and 3D deconvolution (SAFT+Deconv) of ARPAM to improve both lateral and axial resolution in the focus region as well as the out-of-focus region. To our knowledge, this is the first time to show depth-independent deconvolution algorithm for improving both lateral and axial resolution in PA imaging. First, we achieve depth-independent lateral and axial resolution in an extended DOF after 2D SAFT. Then, resolution can be further enhanced with 3D deconvolution using depth-independent PSF. We built a dark-field illumination ARPAM to validate our method [12]. Imaging of 10  $\mu\text{m}$  polymer beads shows that SAFT+Deconv ARPAM improves the lateral resolution from 65–700  $\mu\text{m}$  to 20–29  $\mu\text{m}$ , and the axial resolution from 35–42  $\mu\text{m}$  to 12–19  $\mu\text{m}$  in an extended DOF of  $\sim 2$  mm (from the original DOF of 300  $\mu\text{m}$ ). Phantom imaging of a 3D network of tungsten wires was performed to further confirm the efficacy. *In vivo* imaging of the dorsal subcutaneous microvasculature in a mouse shows that our SAFT+Deconv ARPAM holds promise in revealing subcutaneous microvasculature with deep penetration while high resolution is still maintained.

## 2. Methods

### 2.1. Synthetic aperture focusing technique

In ARPAM, a focused transducer is employed to provide acoustic resolution in the focus region. SAFT can be performed using the VPD concept for a high-NA transducer. The focus of the transducer is considered as VPD to receive ultrasound with a certain solid angle as illustrated in

Fig. 1. If 2D raster scan is performed on the  $xy$  plane (zero of  $z$  coordinate is set at the aperture center of the focused transducer), the superposition of PA radiation pattern from VPDs at adjacent positions facilitates 2D SAFT in the overlapped region above and below the VPD. In 2D SAFT, adjacent positions of the VPDs are used to synthesize the aperture, which is essentially in a circular geometry. The circle is determined by the angular extent of the PA radiation pattern which is basically related to the focusing ability of the ultrasonic transducer. That is, a larger NA of the transducer leads to a bigger aperture that can be synthesized. In our dark-field illumination ARPAM, we built a focused transducer by attaching an acoustic lens (45006, Edmund Optics, NJ) to a 50-MHz flat ultrasonic transducer (V214-BC-RM, 77% bandwidth, Panametrics NDT, MA), which provides an NA of 0.44 and a focal length of 6.7 mm.

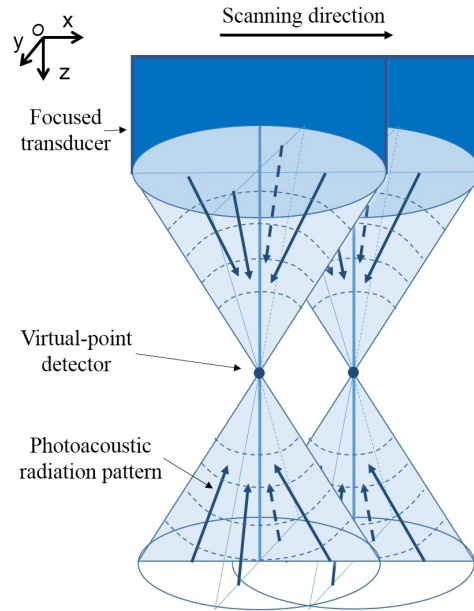


Fig. 1. Schematic of 2D SAFT.

VPD SAFT in fact cannot be applied to the focal point of the transducer as no actual SAFT summing is performed at the focus. SIR of the focused transducer can be used to weight the contributions in SAFT so that we can treat focus and out-of-focus regions in the same way for the SAFT implementation [20]. Mathematically, by applying appropriate time delay relative to the position of VPDs in a circle (i.e., the synthetic aperture) and then summing the delayed signals with corresponding SIR compensations, 2D SAFT can be expressed as follow:

$$S_{SAFT}(x_i, y_j, t_{ij}) = \sum_{i', j'=1}^{circle} S(x_{i'}, y_{j'}, t_{ij} - \Delta t_{i'j'}) SIR(x_{i'} - x_i, y_{j'} - y_j, t_{ij}), \quad (1)$$

where  $S_{SAFT}(x_i, y_j, t_{ij})$  is the signal at a synthetic point  $(x_i, y_j, t_{ij})$  after 2D SAFT,  $S(x_{i'}, y_{j'}, t_{ij})$  is the received signal at the transducer's position  $(x_{i'}, y_{j'})$ ,  $\Delta t_{i'j'}$  is the time delay from the synthetic point to VPDs in the synthetic aperture,  $(x_{i'} - x_i, y_{j'} - y_j, t_{ij})$  is the relative position of the synthetic point to the transducer's position. SIR of the focused transducer is simulated by the DREAM toolbox [30]. Note that the farther the  $z$  position of a synthetic point is away from VPD, the larger the synthetic aperture can be constructed for 2D SAFT and thus a larger number of A-line signals can be incorporated in SAFT.

In addition to 2D SAFT, coherence factor (CF) can further improve the focusing quality by suppressing sidelobes of SAFT images, CF is defined as

$$CF(x_i, y_j, t_{ij}) = \frac{\left| \sum_{i', j'=1}^{circle} S(x_{i'}, y_{j'}, t_{ij} - \Delta t_{i' j'}) SIR(x_{i'} - x_i, y_{j'} - y_j, t_{ij}) \right|^2}{N \sum_{i', j'=1}^{circle} |S(x_{i'}, y_{j'}, t_{ij} - \Delta t_{i' j'}) SIR(x_{i'} - x_i, y_{j'} - y_j, t_{ij})|^2}, \quad (2)$$

where  $N$  is the total number of A-line signals from the transducer's positions located in the synthetic aperture. According to Eq. (2), CF is a real quantity ranging from 0 to 1. Constructive summation of the delayed signals leads to a high value of CF, which indicates that the SAFT image intensity should be maintained, while destructive summation results in a low value of CF, which is used to reduce the SAFT image intensity. After applying the CF map to the SAFT image voxel-by-voxel, the sidelobes in the SAFT image are suppressed and the SNR will also be improved because the noise is generally incoherent. Finally, the CF-weighted 2D SAFT image is obtained as

$$S_{SAFT\_CF}(x_i, y_j, t_{ij}) = S_{SAFT}(x_i, y_j, t_{ij})CF(x_i, y_j, t_{ij}). \quad (3)$$

## 2.2. Richardson-Lucy deconvolution algorithm

If an imaging system is assumed to be linear and space shift-invariant, the output image  $g(x, y, z)$  can be represented as

$$g(x, y, z) = h(x, y, z) \otimes o(x, y, z) + n(x, y, z), \quad (4)$$

where  $h(x, y, z)$  is the PSF of the imaging system,  $\otimes$  stands for convolution operator,  $o(x, y, z)$  is the original true object and  $n(x, y, z)$  is the noise term. The full width at half maximum (FWHM) of the PSF in three dimensions can be considered as the resolution of the imaging system. With a known system PSF, Richardson-Lucy deconvolution algorithm seeks an optimal estimation of the original true object in an iterative way [31, 32], which can be expressed as:

$$o'_{i+1}(x, y, z) = \left[ \frac{g(x, y, z)}{h(x, y, z) \otimes o'_i(x, y, z)} \otimes h(-x, -y, -z) \right] o'_i(x, y, z), \quad (5)$$

where  $i$  is the number of iteration,  $o'(x, y, z)$  is the estimation of original true object, and the initial guess of  $o'_0(x, y, z)$  is usually set as  $g(x, y, z)$ .

Previously we demonstrated 3D deconvolution ARPAM in the focus region [27]. Very similar procedure of the 3D deconvolution is used in this work. The 3D deconvolution is performed in two steps: a one-dimensional (1D) axial deconvolution followed by a 2D lateral deconvolution. The normalized 1D and 2D Gaussian functions with their FWHMs assigned based on the measured axial and lateral resolution of the ARPAM system, respectively, are used as the PSFs in the 3D deconvolution. For convenience, we use a built-in function *deconvlucy* in MATLAB<sup>®</sup> with fixed iteration times to perform the Richardson-Lucy deconvolution algorithm.

Although the axial resolution is generally depth independent in ARPAM, the lateral resolution degrades significantly in the out-of-focus region. The above-mentioned assumption of space shift-invariant in an imaging system becomes invalid when considering the focus and out-of-focus regions simultaneously. In such case, depth-dependent PSFs should be measured if we want to apply deconvolution to the whole image. Fortunately, after 2D SAFT, the lateral resolution becomes depth independent so that both depth-independent axial and lateral PSFs can be used in the 3D deconvolution algorithm with an extended DOF. Additionally, only one measurement in the focus region is sufficient to get the PSF for deconvolution, which elegantly circumvents the challenge caused by many measurements in different layers.

### 3. Results

#### 3.1. Resolution enhancement of SAFT+Deconv ARPAM

We first use 10  $\mu\text{m}$  bead as an approximation of point object to measure the original resolutions of our ARPAM, and then apply 2D SAFT and 3D deconvolution to improve the resolutions.

The bead was embedded in 1% agar and imaged at seven positions (#1~#7) from 5.8 mm to 7.6 mm in depth. The middle one (#4) was in the focal point of the transducer and is to provide the resolution in focal zone. In order to get the original volumetric image, 2D scan was performed with a step size of 10  $\mu\text{m}$ . PA signals were acquired at 200 MS/s without averaging, which corresponds to a depth interval of 7.5  $\mu\text{m}$  in 1D A-line signal considering an acoustic velocity of 1.5 mm/ $\mu\text{s}$  in sound coupling media. Each A-line signal was then interpolated by a factor of 5 to increase the delay accuracy for 2D SAFT. For 2D SAFT, pixel size for the  $x/y$  directions of 5  $\mu\text{m}$  and for the  $z$  direction of 3  $\mu\text{m}$  was used. The XY maximum amplitude projections (MAPs) of object at seven depth positions before and after 2D SAFT are displayed in Figs. 2(a) and 2(b). The #4 sub-image in Fig. 2(b) is different from other sub-images in that column because SAFT has no effect on the focal zone. Note that the scales of Figs. 2(a) and 2(b) are chosen differently for better visualization. Profiles along red dashed lines of object #7 in Fig. 2 are plotted in Fig. 3 to make the quantitative relationship clearer.

In Fig. 2(a), the bead farther away from the focal point has poorer lateral resolution due to limited DOF of the transducer. We check the resolution improvements after 2D SAFT at the seven positions, as listed in Table 1. The lateral resolution denotes the resolution in both  $x$ - and  $y$ -directions as they are symmetrical. The original lateral resolution in the focal zone (65  $\mu\text{m}$ ) is a bit worse than the theoretical value calculated as  $0.71\lambda_0/\text{NA}=49\ \mu\text{m}$ . The original axial resolution (35–42  $\mu\text{m}$ ) agrees well with theoretical value as  $0.88c/B=34\ \mu\text{m}$  where  $B$  is the bandwidth of ultrasonic transducer. After 2D SAFT, the lateral resolution in the focal point remains a constant, whereas the lateral resolutions in the out-of-focus region are improved to basically the same as that in focal zone. Compared with the previous study of 2D SAFT in PAM [18] where SAFT is performed only in two perpendicular directions, our 2D SAFT incorporates all A-line signals within a large circular synthetic aperture determined by the angular extent of the focused transducer, which produces depth-independent lateral resolution in both the focus and out-of-focus regions and a higher SNR improvement. After 2D SAFT, depth-independent lateral resolution of 65–75  $\mu\text{m}$  is obtained. Similar axial resolution of 35–42  $\mu\text{m}$  is obtained because it is determined by the bandwidth of transducer and is inherently depth independent. Depth-independent PSF in both the lateral and axial directions are thus verified and can be used for 3D deconvolution.

Table 1. Resolutions and SNR improvements in SAFT+Deconv ARPAM

Systems	Depth from the transducer (mm)						
	5.8	6.1	6.4	6.7	7	7.3	7.6
Original (lateral/axial, $\mu\text{m}/\mu\text{m}$ )	640/40	380/35	220/42	65/40	220/42	380/42	700/42
2D SAFT ( $\mu\text{m}/\mu\text{m}$ )	70/42	75/42	75/42	65/42	70/39	75/39	75/42
SNR improvement (dB)	23	20	12	0	26	25	31
SAFT+Deconv ( $\mu\text{m}/\mu\text{m}$ )	20/18	21/19	20/19	24/12	29/12	22/15	24/17
SNR improvement (dB)	31	28	17	6	30	31	36

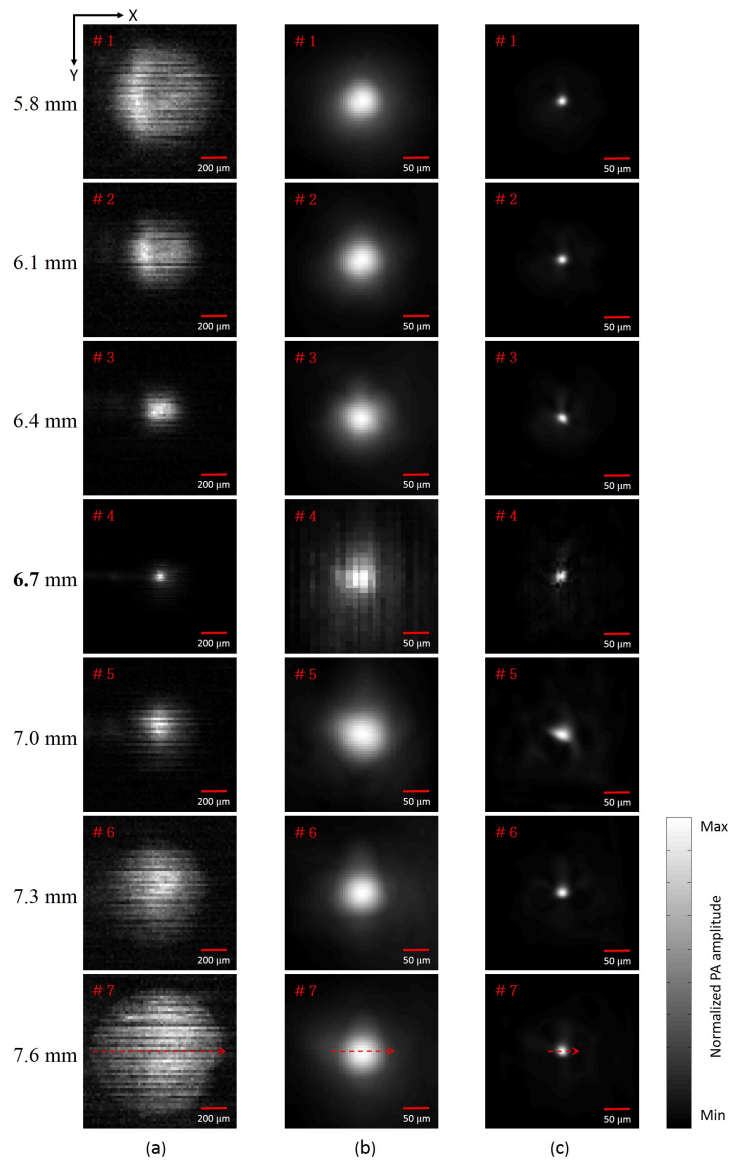


Fig. 2. XY MAPs of the object at seven positions: (a) Original images, (b) 2D SAFT images, and (c) SAFT+Deconv images. The middle object (#4) is placed in the focal zone, the other six objects are placed above (#1–#3) and below (#5–#7) the focal zone. The scale in (a) is 200  $\mu\text{m}$ , while the scales in (b) and (c) are 50  $\mu\text{m}$  for better visualization.

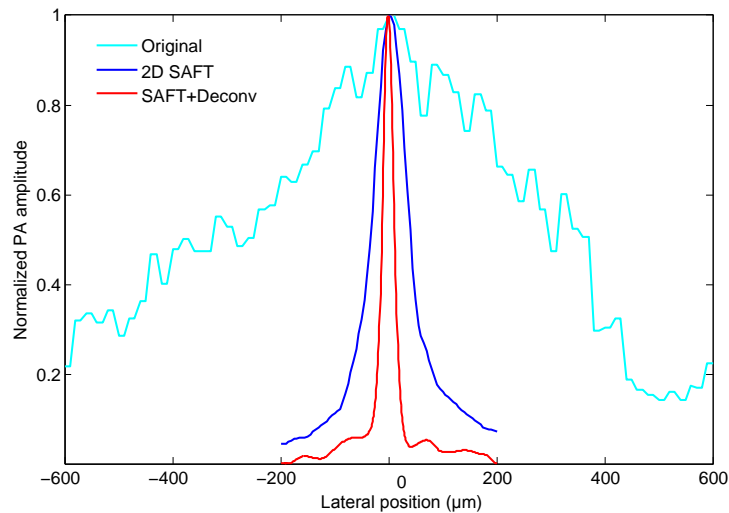


Fig. 3. Profile analysis of three images (#7) along red dashed lines in Fig. 2.

We then performed 3D deconvolution with a pixel size of  $1\ \mu\text{m}$  in three dimensions. The XY MAPs after 3D deconvolution are displayed in Fig. 2(c). The lateral resolution is further improved in both the focus and out-of-focus regions. The reconstructed 2D SAFT and SAFT+Deconv images have better smoothness than the original images due to two factors: (i) the original image has a pixel size of  $10\ \mu\text{m}$ , while the reconstructed SAFT and SAFT+Deconv images have a pixel size of  $5\ \mu\text{m}$  and  $1\ \mu\text{m}$ , respectively; (ii) SAFT and deconvolution algorithms have the effect of making images smoother. Table 1 shows that the lateral resolution is further improved to  $20\text{--}29\ \mu\text{m}$  in an extended DOF of  $\sim 2\ \text{mm}$ . The axial resolution is also enhanced to  $12\text{--}19\ \mu\text{m}$ .

The result also shows improved SNR for SAFT+Deconv images. On one hand, a large number of A-line summations in the synthetic aperture by 2D SAFT suppress the noise by destructive interferences of the noise because it is usually incoherent. Moreover, the object farther away from the focal point shows higher SNR improvement because more A-line signals can be summed in 2D SAFT. On the other hand, deconvolution tends to converge the image intensity to its original sites so that SNR will be improved again for the deconvolved images. SNR improvement of 6 dB for the object in the focal zone arises solely from deconvolution because SAFT has no effect for this region.

### 3.2. Phantom imaging

To further evaluate the efficacy of SAFT+Deconv ARPAM, we imaged a phantom composed of  $25\text{-}\mu\text{m}$  tungsten wires with different orientations and depths to simulate the distribution of vascular networks. The phantom was placed  $\sim 600\ \mu\text{m}$  below the focus of the transducer to better demonstrate resolution enhancement in SAFT+Deconv ARPAM. The area of 2D scan was  $4 \times 4\ \text{mm}^2$  with a step size of  $20\ \mu\text{m}$ .

Figures 4 and 5 show the XY and YZ MAPs, respectively, of the original, 2D SAFT and SAFT+Deconv images. In Fig. 4, the enhanced lateral resolution by SAFT+Deconv ARPAM enables clearer identification of the wire pattern. As shown in Fig. 4(a), the tungsten wires at different depths have different lateral widths and their signal amplitudes also varies with depths. After 2D SAFT, the lateral resolution is improved to the same level for all the five tungsten wires and more details of the phantom can be revealed such as in the regions enclosed by the white boxes 1 (B1) and 2 (B2) in Fig. 4. For the region B1, due to the poor resolution in the out-of-focus region, the tungsten wire pattern in B1 of Fig. 4(a) can hardly be identified. After

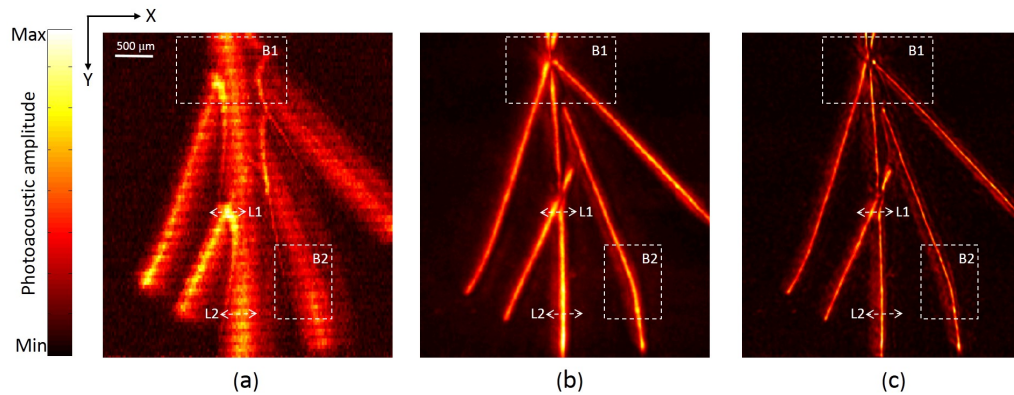


Fig. 4. XY MAPs of five 25- $\mu\text{m}$  tungsten wires: (a) Original image, (b) 2D SAFT image, and (c) SAFT+Deconv image.

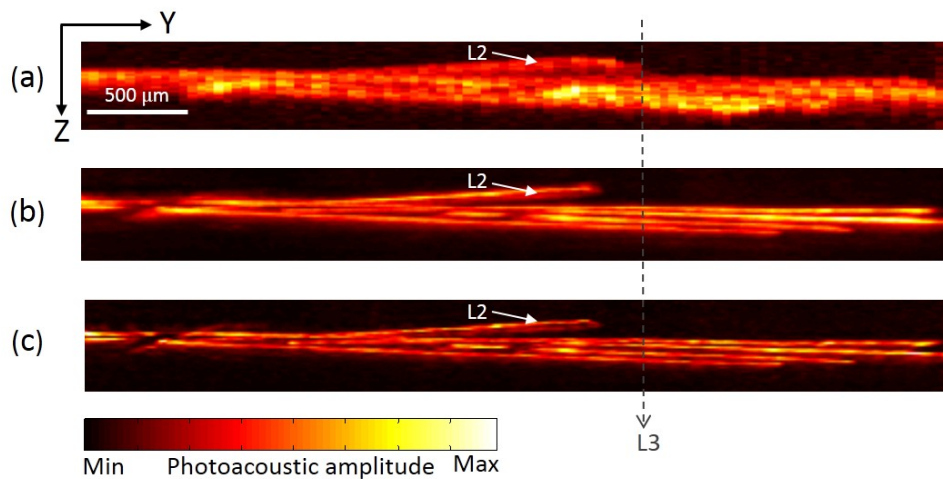


Fig. 5. YZ MAPs of five 25- $\mu\text{m}$  tungsten wires: (a) Original image, (b) 2D SAFT image, and (c) SAFT+Deconv image.

2D SAFT, the joint and branches of the tungsten wires emerge in B1 of Fig. 4(b). After 3D deconvolution, an even clearer pattern can be identified in B1 of Fig. 4(c). For the region B2, the tungsten wire in B2 of Fig. 4(a) seems to be straight, while the orientation is better revealed in B2 of Fig. 4(b) after 2D SAFT. After 3D deconvolution, a slight bend can be clearly observed in B2 of Fig. 4(c) because the lateral resolution is further improved. We also check the lateral profile (Fig. 6(a)) of the imaged tungsten wires along the white line L1 labeled in Fig. 4. As shown in Fig. 6(a), the two closely-arranged tungsten wires merge as one and cannot be distinguished in the original image. We can then readily identify these two tungsten wires in the 2D SAFT image. The 3D deconvolution further restores the lateral width of the tungsten wires and thus enhances the visibility of two close tungsten wires. The diameters of tungsten wires labeled by white line L2 in Fig. 4 are 400  $\mu\text{m}$  (Original), 80  $\mu\text{m}$  (2D SAFT), and 35  $\mu\text{m}$  (SAFT+Deconv), and the 35  $\mu\text{m}$  is quite close to the true tungsten wire's diameter of 25  $\mu\text{m}$ . Both 2D SAFT and 3D deconvolution enhance the contrast of the two close tungsten wires as the background noise is reduced. Compared with the original image, the SAFT+Deconv image has an overall SNR

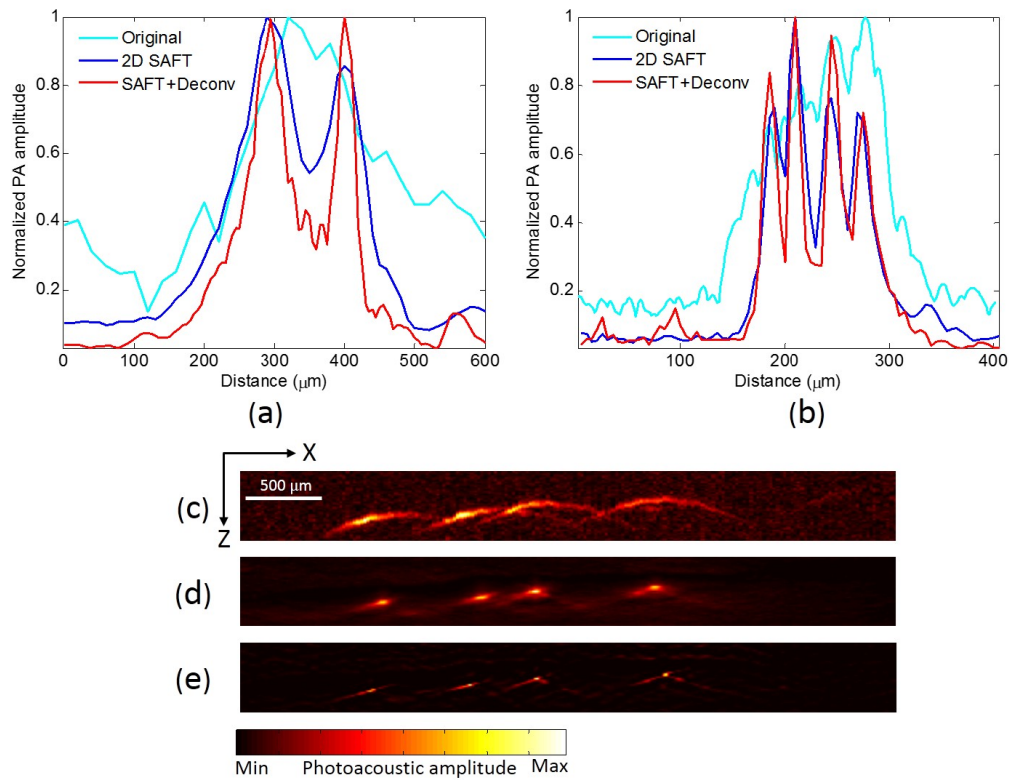


Fig. 6. (a) Lateral profile along the line L1 in Fig. 4. (b) Axial profile along the line L3 in Fig. 5. (c)–(e) XZ cross-sectional images from the region labeled by the line L3 in Fig. 5.

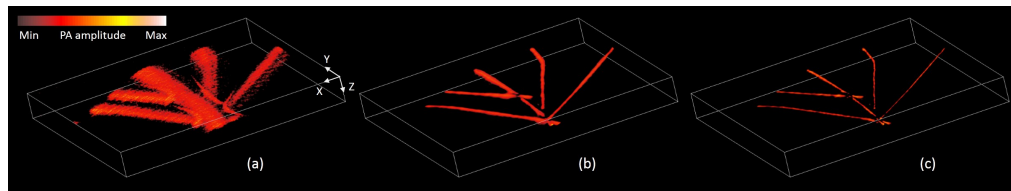


Fig. 7. 3D rendering display of five 25- $\mu\text{m}$  tungsten wires: (a) Original image, (b) 2D SAFT image, and (c) SAFT+Deconv image.

improvement of  $\sim 20$  dB.

In Fig. 5, it is impossible to distinguish the five tungsten wires in the original image in Fig. 5(a) due to both the wide lateral extent and poor axial resolution. After 2D SAFT, a better identification can be achieved in Fig. 5(b). The tungsten wires labeled by L2 can now be identified, but the rest four tungsten wires are still mixed together due to poor axial resolution. Furthermore, the axial resolution is enhanced by 3D deconvolution and thus, we can clearly identify the four closely-arranged tungsten wires in the axial direction from Fig. 5(c). The change along the axial direction among the original, 2D SAFT, and SAFT+Deconv images can also be observed by checking the axial profile of the imaged tungsten wires along the dashed line L3 in Fig. 5, which is plotted in Fig. 6(b). From Fig. 6(b), after 2D SAFT a better identification of the four tungsten wires in the axial direction is achieved, which is not due to the improved axial resolution but the reduced lateral extent of the tungsten wires from the original image since 2D SAFT does not

improve the axial resolution of the original image.

To better understand Fig. 6(b), we check the XZ cross-sectional images of the original, 2D SAFT, and SAFT+Deconv images (shown in Figs. 6(c)–6(e), respectively) sliced from the region labeled by the dashed line L3 in Fig. 5. In Fig. 6(c), because the phantom was placed below the focal point of the transducer, the original image of the four tungsten wires exhibit wide downward arch-shaped profile, which overlaps with each other in the  $z$  direction for the original YZ MAP in Fig. 5(a). In Fig. 6(d), the wide lateral extent of the original image is narrowed after 2D SAFT, resulting in less overlaps in the  $z$  direction, and thus, we can better distinguish the four tungsten wires in Fig. 5(b). In Fig. 6(e), both the lateral and axial resolution are improved after 3D deconvolution, and therefore, even better visibility of the four tungsten wires can be acquired in Fig. 5(c). However, as shown in Figs. 4(c) and 6(e), the deconvolution also introduces speckles which degrade the image quality. The deconvolved image after many iterations shows a speckled appearance due to noise amplification. Noise amplification is a general problem for all maximum likelihood techniques (e.g. Richardson-Lucy algorithm), which attempts to fit the data as closely as possible.

To better show the phantom imaging result by SAFT+Deconv ARPAM, volumetric 3D rendering display of the original, 2D SAFT, and SAFT+Deconv images are presented in Figs. 7(a)–7(c), respectively. A clear improvement of spatial resolution in both the lateral and axial directions can be seen in the SAFT+Deconv ARPAM image in Fig. 7(c).

### 3.3. *In vivo* imaging

We also conducted *in vivo* experiments with a mouse to further evaluate the efficacy of the proposed SAFT+Deconv ARPAM. The laboratory animal protocol for this research was approved by Laboratory Animal Care Committee of Shanghai Jiao Tong University. The vascular distribution in the dorsal subcutaneous vessels of a BALB/c mouse ( $\sim 20$  g; Slac Laboratory Animals) was imaged. Before imaging, we administered a dose of 100 mg/kg pentobarbital intramuscularly to anesthetize the animal and removed the hair from the region of interest by a human hair-removal lotion. For *in vivo* imaging, the optical fluence deposited on the biological tissue was  $\sim 7$  mJ/cm<sup>2</sup>, which is under the ANSI safety limit (20 mJ/cm<sup>2</sup>). A 2D scan of  $8 \times 6$  mm<sup>2</sup> was then performed with step size of 40  $\mu$ m to reduce the scanning time. The mouse revived about one hour after 2D scan and was sent back to the laboratory animal care center.

Figures 8(a)–8(c) show XY MAPs of vascular distribution in the original, 2D SAFT, and SAFT+Deconv images, respectively. For the 3D network of vessels, it is imaged in both the focal and out-of-focus regions as shown in the depth-encoded XY MAP in Fig. 8(e). The vessel pattern in Fig. 8(b) after 2D SAFT can be more clearly identified because of the improved lateral resolution and enhanced image contrast. Furthermore, the contrast of vessels enclosed by white dashed boxes B1 and B2 is especially enhanced in the 2D SAFT image due to a larger number of summation ( $N$ ) for SAFT in the out-of-focus region. In Fig. 8(c), the resolution is further improved in the SAFT+Deconv image. To better show the unique advantage of SAFT+Deconv ARPAM, we processed the original image with just 3D deconvolution and the XY MAP is showed in Fig. 8(d). Compared with Fig. 8(d), Fig. 8(c) shows a higher contrast and better resolution improvement. For the original ARPAM, system PSF varies along the depth. Performing 3D deconvolution in the out-of-focus region using PSF in the focal zone will thus cause reconstruction error. SAFT+Deconv ARPAM, however, can use a depth-independent PSF to both the focal zone and out-of-focus region due to depth-independent lateral resolution after 2D SAFT.

We further check the XZ cross-sectional images (Figs. 8(a)–8(c)) from the slices labeled by the white dashed lines L1 in Figs. 8(a)–8(c), respectively, to manifest the improvement by the SAFT+Deconv ARPAM. In Fig. 9(a), the vessels labeled by  $V_1$ – $V_3$  have wider lateral extent compared with the near-focus vessel labeled by  $V_4$ . In Fig. 9(b), vessels  $V_1$ – $V_3$  can be more clearly

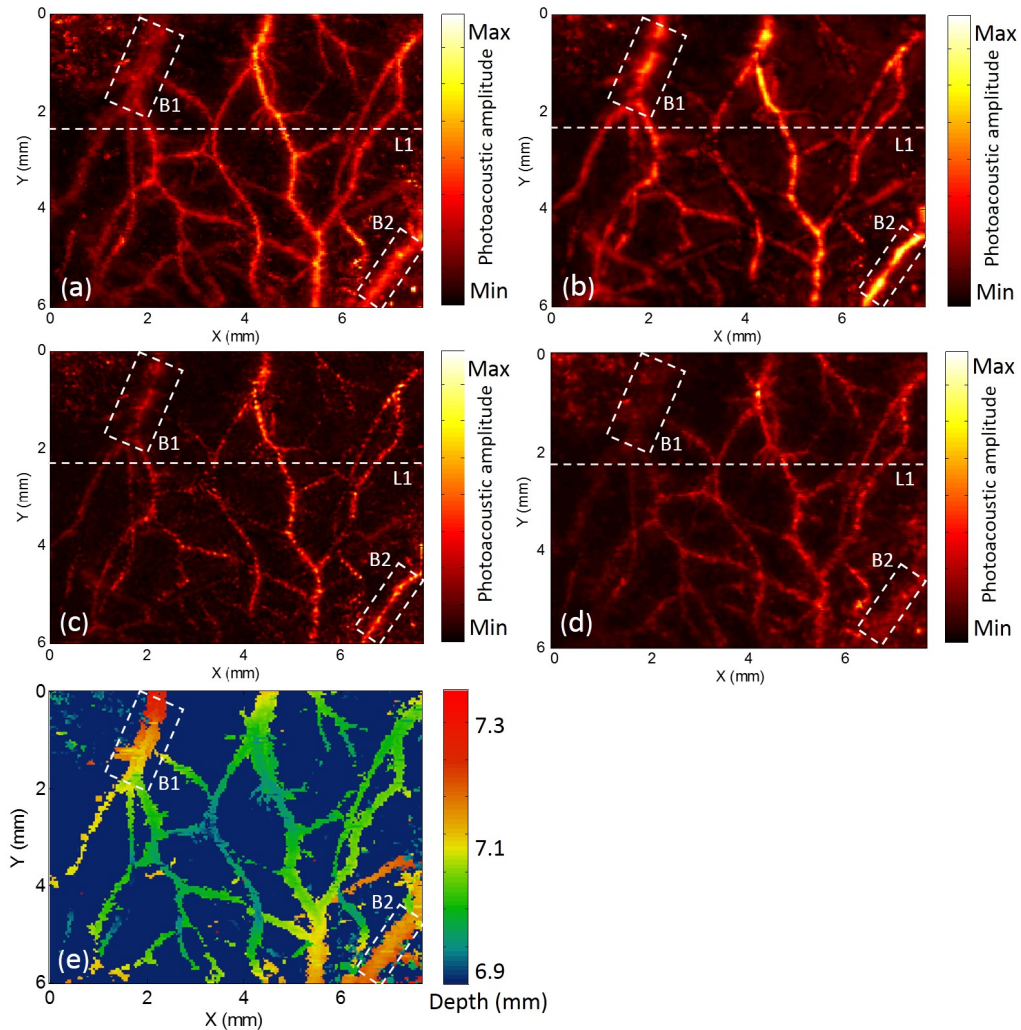


Fig. 8. XY MAPs of *in vivo* imaging of a mouse's dorsal subcutaneous vessels: (a) Original image, (b) 2D SAFT image, (c) SAFT+Deconv image, (d) Deconvolution image, and (e) Depth-encoded XY MAP.

identified due to the improved lateral resolution and contrast by 2D SAFT. In Fig. 9(c), further improved lateral and axial resolution and enhanced contrast after 3D deconvolution enable an even better identification of all the vessels no matter what depths they are in.

#### 4. Discussions

2D SAFT can be performed either in two perpendicular directions [18] or in a circle. In this work, we performed 2D SAFT in a circle so that depth-independent lateral resolution can be achieved for point objects as shown in beads phantom imaging. Unlike the spherical wavefront emitted from beads, the cylindrical wavefront from line objects results in mismatch between PA signal and the spherically focused transducer. We observe that certain details are lost in the 2D SAFT image of Fig. 8, which may be attributed to three factors: (i) Highly inhomogeneous and anisotropic biological tissue tortures the propagation of ultrasound and thus cause the deviation from the theoretical model for 2D SAFT; (ii) Low-coherent background noise from capillaries

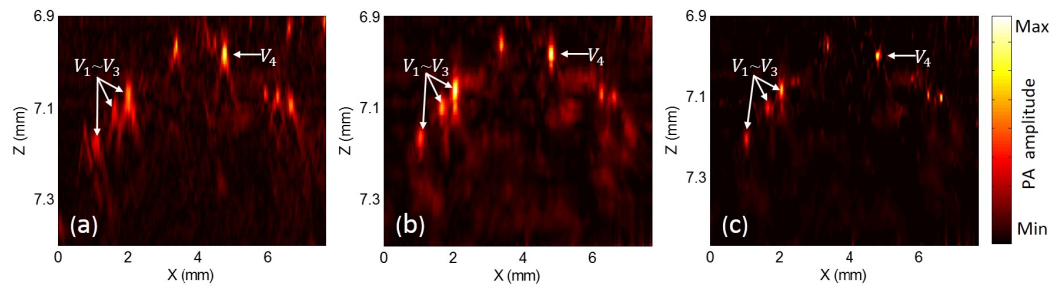


Fig. 9. (a)–(c) are XZ cross-sectional images from slices labeled by white dashed lines L1 in Figs. 8(a)–8(c), respectively.

are also enhanced, which may suppress certain details; (iii) Mismatch between the cylindrical PA wavefront and the spherically focused transducer. In this work, we mainly validate SAFT+Deconv using point objects where Richard-Lucy deconvolution algorithm is best suited. For the line objects, especially for the vessel network, adaptive SAFT has proven to be more effective to restore the degraded lateral resolution in the out-of-focus region [19]. ASAFT combined with deconvolution then could be good future work for line object restoration. Focused transducer with higher center frequency and higher NA may also be adopted to resolve much smaller structures currently taken as background noise.

The *in vivo* SAFT+Deconv image shows discontinuity and degraded SNR which are not presented in *in vitro* phantom results. The reasons for the discrepancy between *in vitro* results and *in vivo* results are as follows: (i) The *in vitro* result has higher SNR than the *in vivo* result which is limited by the ANSI laser safety standard. The higher SNR of the original image, the better image quality after SAFT+Deconv. (ii) The *in vitro* phantom is composed of simple uniform tungsten wires with diameters of 25  $\mu\text{m}$ , while the *in vivo* microvasculature has a complex network of vessels with different diameters ranging from capillaries of several micrometers to big vessels of nearly one hundred micrometers. The Richard-Lucy deconvolution algorithm we used was initially developed to deblur point objects for an astronomical purpose, and thus, line objects such as the vessel have the tendency to be deconvolved to many discrete point objects. Also noise amplification of maximum likelihood techniques (e.g. the Richard-Lucy algorithm) causes speckled appearances [33]. The damped Richard-Lucy algorithm may also be useful to suppress the speckle. Introduction of a regularized term in deconvolution algorithm may be used to maintain or even better recognize the vessel pattern [34].

## 5. Conclusions

In this work, we combined 2D SAFT and 3D deconvolution to improve spatial resolution in three dimensions both in the focus and out-of-focus regions in ARPAM. Depth-independent lateral and axial resolution after 2D SAFT provides a depth-independent PSF for 3D deconvolution, which significantly eases the effort in the calibration of PSFs since only one PSF at the focus region should be measured. By imaging of 10  $\mu\text{m}$  beads, the  $-6$  dB lateral resolution is improved from 65–700  $\mu\text{m}$  to 20–29  $\mu\text{m}$  and the axial resolution from 35–42  $\mu\text{m}$  to 12–19  $\mu\text{m}$  in an extended DOF of  $\sim 2$  mm. The SNR is also increased. Imaging of the network of the tungsten wires validates the feasibility of SAFT+Deconv ARPAM for microvascular imaging. *In vivo* imaging of the dorsal subcutaneous microvasculature is further conducted to show the promise of the proposed SAFT+Deconv ARPAM. There are still some issues for *in vivo* experiments, such as degraded SNR and lost small structures in some regions. Tackling the *in vivo* issues may be a future direction for this work as listed: (i) A focused transducer with higher center frequency (e.g., 75 MHz) and a higher NA to reveal even finer structure; (ii) Adaptive SAFT to have better

image restoration for line objects in the out-of-focus region; (iii) Introduction of regularized term in deconvolution algorithm to maintain or even better recognize the vessel pattern while mitigating speckle issues.

### **Funding**

This work was supported by National Natural Science Foundation of China (NSFC) (61405112); National High Technology Research and Development Program of China (863 Program) (2015AA020944); Shanghai Science and Technology Committee (STCSM) (15140901400).